Ca2+ as cofactor of the mitochondrial H+-translocating F1FO-ATP(hydrol)ase

(Article begins on next page)

22 September 2024

Thermally unstable throughflow of a power–law fluid in a vertical porous cylinder with arbitrary cross–section

P.V. Brandão[a,*], M. Celli[a], A. Barletta[a] and L. Storesletten[b]

[a]*Alma Mater Studiorum Università di Bologna, Department of Industrial Engineering, Viale Risorgimento 2, 40136 Bologna, Italy*
[b]*Department of Mathematics, University of Agder, Postboks 422, 4604 Kristiansand, Norway*

ARTICLE INFO

ABSTRACT

The present paper investigates how the cross–sectional shape of a vertical porous cylinder affects the onset of thermoconvective instability of the Rayleigh–Bénard type. The fluid saturating the porous medium is assumed to be a non–Newtonian power–law fluid. A linear stability analysis of the vertical thorughflow is carried out. Three special shapes of the cylinder cross–section are analysed: square, circular and elliptical. The effect of changing the power–law index is investigated. The stability of a steady base state with vertical throughflow is analysed. The resulting stability problem is a differential eigenvalue problem that is solved numerically through the shooting method. The dimensionless numbers here considered are the non–Newtonian version of the Darcy–Rayleigh number, Ra, the Péclet number, Pe and the power–law index, n. Results are presented in the form of marginal stability curves with Ra plotted as a function of the cylinder aspect ratio, by assuming different values of Pe and n. The critical values of Ra are also computed. Results show that the critical Rayleigh number Ra for instability depends only on Pe and n, and is independent of the shape of the cylinder cross–section. The geometry of the sidewall just contributes the selection of the allowed wavenumbers.

1. Introduction

The thermoconvective instability is of interest in a wide range of scientific and engineering applications involving fluid systems subject to an externally imposed temperature gradient. Depending on the nature of the process, it can be desirable or not to enhance the heat transfer caused by free or mixed convection. In the last century, many studies have been carried out where the linear stability theory is employed to investigate the onset of convection in such systems.

In the context of porous media, the pioneering investigations of the onset of convection in a layer of fluid heated from below, by means of linear stability theory, were first reported by [9] and by [10]. In a later study, [13] investigated the effect of a horizontal throughflow in the transition to instability, reaching the conclusion that throughflow does not affect the transition to the convective instability. Then [16] and [8] extended these classical results by considering the horizontal walls as permeable and devising the presence of a vertical throughflow.

As mentioned by [14] in his book, convection heat transfer may be of interest also when non–Newtonian fluids saturate porous media. Processes involving oil recovery and its enhancement, or filtration and ceramic processing are examples of non–Newtonian flows in porous media.

More recently, several studies have been done in this direction including more complex effects. [4] investigated the effect of vertical throughflow on the onset of convection in a horizontal porous channel, by taking into consideration the effect of heat generated by viscous dissipation inside the channel. Then, [2] investigated the role of a non–Newtonian rheology on the transition to instability, but yet considering horizontal throughflow. [6] investigated the effect of vertical throughflow on the onset of instability for power–law fluids.

The present paper aims to study the effect of the lateral confinement on the transition to instability for vertical throughflow in a horizontal porous channel saturated by non–Newtonian fluid of power–law type. In their paper, [5] have already concluded, for the special case of a Newtonian fluid, that the geometry of a vertical permeable and conducting cylinder does not affect the eigenvalue problem solution and, consequently, the onset of instability. Although this conclusion can be expected to hold also for a more complex fluid rheology, this topic is well worth to be investigated rigorously. In order to carry out such an investigation, a linear stability analysis is employed. This analysis consists in defining first a stationary base solution of the governing equations. Hence, by introducing small–amplitude perturbations of the base state, we determine their evolution in time. In fact, this study deals with the linearisation of the governing equations for the perturbations and the numerical solution of the stability differential eigenvalue problem.

2. Mathematical Model

Throughflow in a vertical porous cylinder saturated by an Ostwald–de Waele (power–law) fluid is considered. The cylinder is bounded by two horizontal permeable planes, and a lateral sidewall with an arbitrary cross–section. Let the vertical z axis be parallel to the gravitational acceleration **g**, but with opposite direction (see figure 1). The sidewall boundary is impermeable and adiabatic, while the horizontal boundary planes, at $z = 0$ and $z = H$, are permeable and isothermal with temperatures $T = T_0 + \Delta T$ and $T = T_0$, respectively. Here, T is the temperature field, T_0 is a reference temperature and ΔT is a positive temperature difference.

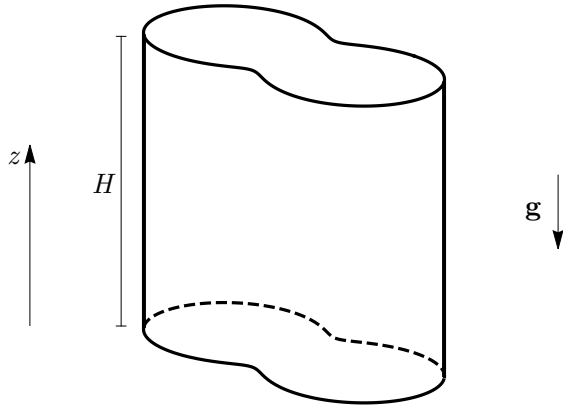*corresponding author: pedro.vayssiere2@unibo.it
ORCID(s):

Figure 1: Sketch of the porous cylinder laterally confined by an arbitrarily shaped sidewall

2.1. Governing Equations

When a power–law fluid saturates a porous medium and the flow is driven by the thermal buoyancy force, the appropriate model can be based on the Oberbeck–Boussinesq approximation and on the generalized Darcy's law [14, 7]. The generalised Darcy's law, together with the equations for local mass balance and energy balance, yield

$$\boldsymbol{\nabla} \cdot \mathbf{u} = 0, \tag{1a}$$

$$\frac{\mu^*}{K} |\mathbf{u}|^{n-1} \mathbf{u} = -\boldsymbol{\nabla} p - \rho_0 \mathbf{g} \beta (T - T_0), \tag{1b}$$

$$\sigma \frac{\partial T}{\partial t} + \mathbf{u} \cdot \boldsymbol{\nabla} T = \kappa \nabla^2 T, \tag{1c}$$

where $\mathbf{u}$ is the velocity with Cartesian components (u, v, w), μ^* is the effective consistency factor (with SI units $\mathrm{Pa}\,\mathrm{s}^n\,\mathrm{m}^{1-n}$), K is the permeability (with SI units m^2) and p is the local difference between the pressure and the hydrostatic pressure, ρ_0 is the density of the fluid at temperature T_0, while β is the thermal expansion coefficient of the fluid. Time is denoted by t, σ is the ratio between the average volumetric heat capacity of the saturated porous medium and the volumetric heat capacity of the fluid and κ is the effective thermal diffusivity of the porous medium. The effective consistency factor μ^* depends on the consistency factor of the power–law fluid, on the power–law index n, on the permeability K, as well as on the porosity and on the tortuosity [14, 7]. The generalised Darcy's law (1b) was previously employed, for instance, in the convective instability study carried out by [6].

The lateral sidewall consists of a vertical cylinder whose cross–section A is bounded by a closed, piecewise differentiable curve ∂A in the (x, y) plane. The curve ∂A is defined by the equation

$$F(x, y) = 0. \tag{2}$$

A vertical throughflow in the porous cylinder is induced by the following boundary conditions:

$$z = 0, \quad x, y \in A : \quad w = w_0, \quad T = T_0 + \Delta T, \tag{3a}$$

$$z = H, \quad x, y \in A : \quad w = w_0, \quad T = T_0, \tag{3b}$$

$$F(x, y) = 0, \quad 0 < z < H : \quad \mathbf{n} \cdot \mathbf{u} = \mathbf{n} \cdot \boldsymbol{\nabla} T = 0, \tag{3c}$$

where w_0 is the prescribed vertical throughflow velocity and $\mathbf{n}$ is the unit outward normal to the cylinder sidewall. Thus, $\mathbf{n}$ lies on the (x, y) plane.

2.2. Dimensionless quantities

We now scale the dimensional quantities and operators in order to define a dimensionless formulation

$$\frac{1}{H}\mathbf{x} \to \mathbf{x}, \quad \frac{H}{\kappa}\mathbf{u} \to \mathbf{u}, \quad \frac{\kappa}{\sigma H^2} t \to t,$$
$$\frac{T - T_0}{\Delta T} \to T, \quad H\boldsymbol{\nabla} \to \boldsymbol{\nabla}, \quad H^2 \nabla^2 \to \nabla^2. \tag{4}$$

The dimensionless parameters Ra and Pe are defined as

$$Ra = \frac{\rho_0 g \beta \Delta T K H^n}{\mu^* \kappa^n}, \quad Pe = \frac{w_0 H}{\kappa}, \tag{5}$$

where g is the modulus of $\mathbf{g}$. The dimensionless parameter Ra is the non–Newtonian version of the Darcy–Rayleigh number, while Pe is the Péclet number. The instability is possible only if Ra is positive. On the other hand, either sign of Pe is possible with a positive Pe yielding upward throughflow and a negative Pe meaning downward throughflow. By employing the dimensionless quantities defined by equations (4) and (5), equations (1) can be written as

$$\boldsymbol{\nabla} \cdot \mathbf{u} = 0, \tag{6a}$$

$$\boldsymbol{\nabla} \times (|\mathbf{u}|^{n-1}\mathbf{u}) = Ra\boldsymbol{\nabla} \times (T\mathbf{e}_z), \tag{6b}$$

$$\frac{\partial T}{\partial t} + \mathbf{u} \cdot \boldsymbol{\nabla} T = \nabla^2 T, \tag{6c}$$

where $\mathbf{e}_z$ is the unit vector in the z direction. Equation (6b) was obtained by applying the curl operator to both sides of equation (1b), so that the dynamic pressure field is eliminated from the governing equations. The dimensionless boundary conditions (3) can be rewritten in a dimensionless form as

$$z = 0, \quad x, y \in A : \quad w = Pe, \quad T = 1, \tag{7a}$$

$$z = 1, \quad x, y \in A : \quad w = Pe, \quad T = 0, \tag{7b}$$

$$F(x, y) = 0, \quad 0 < z < 1 : \quad \mathbf{n} \cdot \mathbf{u} = \mathbf{n} \cdot \nabla T = 0. \quad (7c)$$

We note that, for the sake of simplicity, we use the same notation for the dimensionless equation, $F(x, y) = 0$, as that employed to characterise the dimensional boundary in the (x, y) plane. Obviously, in the former case we deal with dimensionless coordinates. Furthermore, the function F itself is different from that employed with dimensional coordinates, unless F is homogeneous, which is a special case. Accordingly, we will also continue to call A and ∂A the dimensionless cross–section of the cylinder and its boundary, respectively.

2.3. Base flow state

A stationary solution of equations (6) and (7) is given by a uniform vertical throughflow with a purely vertical temperature gradient dT_b/dz, namely

$$u_b = 0, \quad v_b = 0, \quad w_b = Pe, \quad T_b(z) = \frac{e^{Pe} - e^{Pez}}{e^{Pe} - 1}. \quad (8)$$

where the subscript "b" stands for base flow state.

3. Small–amplitude perturbations

A stability analysis of the vertical base throughflow is now carried out under the assumption of small–amplitude perturbations.

3.1. Disturbance equations

Stability is studied by perturbing the basic solution (8). The velocity and temperature fields are then expressed as

$$\mathbf{u} = Pe\,\mathbf{e}_z + \epsilon\tilde{\mathbf{u}}, \quad T = T_b(z) + \epsilon\tilde{T}, \quad (9)$$

where $\tilde{\mathbf{u}} = (\tilde{u}, \tilde{v}, \tilde{w})$ and $\tilde{T}$ are the perturbation fields, while $\epsilon > 0$ is an infinitesimal perturbation parameter such that, hereafter, terms $O(\epsilon^2)$ are considered as negligible.

Thus, substitution of equation (9) into equations (6) yields a linearised system of governing equations given by

$$\frac{\partial \tilde{u}}{\partial x} + \frac{\partial \tilde{v}}{\partial y} + \frac{\partial \tilde{w}}{\partial z} = 0, \quad (10a)$$

$$n\frac{\partial \tilde{w}}{\partial y} - \frac{\partial \tilde{v}}{\partial z} = \frac{Ra}{|Pe|^{n-1}}\frac{\partial \tilde{T}}{\partial y}, \quad (10b)$$

$$n\frac{\partial \tilde{w}}{\partial x} - \frac{\partial \tilde{u}}{\partial z} = \frac{Ra}{|Pe|^{n-1}}\frac{\partial \tilde{T}}{\partial x}, \quad (10c)$$

$$\frac{\partial \tilde{v}}{\partial x} - \frac{\partial \tilde{u}}{\partial y} = 0, \quad (10d)$$

$$\frac{\partial \tilde{T}}{\partial t} + \tilde{w}\frac{\partial T_b}{\partial z} + Pe\frac{\partial \tilde{T}}{\partial z} = \nabla^2 \tilde{T}, \quad (10e)$$

which are subject to the boundary conditions

$$z = 0, 1, \quad x, y \in A : \quad \tilde{w} = \tilde{T} = 0, \quad (11a)$$

$$F(x, y) = 0, \quad 0 < z < 1 : \quad \mathbf{n} \cdot \tilde{\mathbf{u}} = \mathbf{n} \cdot \nabla\tilde{T} = 0. \quad (11b)$$

For practical reasons, it is convenient to rewrite the linearised equations according to a $\tilde{w}$–$\tilde{T}$ formulation. Thus, by rearranging equations (10) and (11), we have

$$n\left(\frac{\partial^2 \tilde{w}}{\partial x^2} + \frac{\partial^2 \tilde{w}}{\partial y^2}\right) + \frac{\partial^2 \tilde{w}}{\partial z^2} = \frac{Ra}{|Pe|^{n-1}}\left(\frac{\partial^2 \tilde{T}}{\partial x^2} + \frac{\partial^2 \tilde{T}}{\partial y^2}\right), \quad (12a)$$

$$\frac{\partial \tilde{T}}{\partial t} + \tilde{w}\frac{dT_b}{dz} + Pe\frac{\partial \tilde{T}}{\partial z} = \frac{\partial^2 \tilde{T}}{\partial x^2} + \frac{\partial^2 \tilde{T}}{\partial y^2} + \frac{\partial^2 \tilde{T}}{\partial z^2}. \quad (12b)$$

$$z = 0, 1, \quad x, y \in A : \quad \tilde{w} = \tilde{T} = 0, \quad (12c)$$

$$F(x, y) = 0, \quad 0 < z < 1 : \quad \mathbf{n} \cdot \nabla\tilde{w} = \mathbf{n} \cdot \nabla\tilde{T} = 0. \quad (12d)$$

With the new formulation, all the boundary conditions must be expressed in terms of $\tilde{w}$ and $\tilde{T}$, as in equation (12d). In particular, the boundary condition for $\tilde{w}$ in equation (12d) can be proved by evaluating the scalar product of the momentum balance equation in the (x, y) plane, expressed through equations (10b) and (10c), with the unit normal $\mathbf{n}$ to the curve ∂A, namely

$$n\,\mathbf{n} \cdot \nabla\tilde{w} - \frac{\partial (\mathbf{n} \cdot \tilde{\mathbf{u}})}{\partial z} = \frac{Ra}{|Pe|^{n-1}}\,\mathbf{n} \cdot \nabla\tilde{T}. \quad (13)$$

Thus, by employing equation (13) for $(x, y) \in \partial A$, if we take into account equation (11b), then we obtain

$$\mathbf{n} \cdot \nabla\tilde{w} = 0, \quad (14)$$

which is the boundary condition for $\tilde{w}$ reported in equation (12d).

3.2. Eigenvalue problem

In order to detect the parametric threshold for the onset of instability, *i.e.* the neutral stability condition, we consider disturbances expressed as normal modes periodic in time,

$$\tilde{T} = \Theta(z) f(x, y)\, e^{i\,\omega t}, \quad (15a)$$

$$\tilde{w} = W(z) f(x, y)\, e^{i\,\omega t}, \quad (15b)$$

where ω is the angular frequency. Here, $f(x, y)$ is a solution of the two–dimensional Helmholtz equation with Neumann boundary conditions at $F(x, y) = 0$, namely

$$\nabla^2_2 f(x, y) = -\alpha^2 f(x, y), \quad (16a)$$

Table 1

Square cross–section: first 11 modes and the corresponding eigenvalues (22).

(m_1, m_2)	$\alpha\ell$
(0,0)	0
(1,0)	3.14159
(1,1)	4.44288
(2,0)	6.28319
(2,1)	7.02481
(2,2)	8.88577
(3,0)	9.42478
(3,1)	9.93459
(3,2)	11.3272
(4,0)	12.5664
(4,1)	12.9531

$$F(x, y) = 0 : \quad \mathbf{n} \cdot \nabla f(x, y) = 0, \tag{16b}$$

where α is the wavenumber. Due to the symmetry under rotations around the z axis displayed both by the governing equations and by the basic flow state, the principle of exchange of stabilities is expected to hold (see, for instance, Alves and Barletta 2, Barletta and Storesletten 6). Thus, we can set $\omega = 0$, although this result cannot be proved theoretically for the present problem. However, the validity of the principle will be verified numerically for every case examined in the following. By employing equations (15) and (16), equations (12) yield

$$W'' - n\,\alpha^2\,W + \frac{Ra}{|Pe|^{n-1}}\,\alpha^2\,\Theta = 0, \tag{17a}$$

$$\Theta'' - Pe\,\Theta' - (\alpha^2 + i\omega)\,\Theta + Pe\,G(z)\,W = 0, \tag{17b}$$

$$z = 0, 1 : \quad W = \Theta = 0, \tag{17c}$$

Here, the primes denote differentiation with respect to z and $G(z)$ is defined as

$$G(z) = -\frac{1}{Pe}\frac{dT_b}{dz} = \frac{e^{Pez}}{e^{Pe} - 1}. \tag{18}$$

By looking into the eigenvalue problem defined by equations (17) some conclusions can be drawn regarding the role played by the sign of Pe. In principle, Pe may assume either positive or negative values, which corresponds to upward or downward flow, respectively. By inspecting equations (17), one may observe that just equation (17b) is affected by a sign change of Pe, while in equation (17a) Pe appears with its absolute value. For a downward flow, i.e. negative Pe, by applying a simple coordinate transformation, it can be seen that the eigenvalue problem is mapped onto one with a positive Pe. In fact, on account of equation (18), the eigenvalue problem (17) remains invariant under the transformation

$$Pe \to -Pe, \qquad z \to 1 - z. \tag{19}$$

As already pointed out by Barletta and Storesletten [6], the practical effect of this symmetry is that the eigenvalue, i.e. the pair (ω, Ra), does not depend on the sign of Pe, while the eigenfunctions (W, Θ) undergo a reflection with respect to the midplane $z = 1/2$. Thus, hereafter, only positive values of Pe will be considered without any loss of generality.

3.3. Three special cases

Three different cases for the lateral confinement are considered here, namely

1. A is a square, with dimensionless side length ℓ;
2. A is a circle with dimensionless radius s. In other terms, ∂A is defined by the equation $F(x, y) = x^2 + y^2 - s^2 = 0$;
3. A is an ellipse with dimensionless semiaxes b and d, with $b > d$. In this case, ∂A is given by $F(x, y) = x^2/b^2 + y^2/d^2 - 1 = 0$.

Table 2

Circular cross–section: first 11 modes and the corresponding eigenvalues (25).

(m, k)	$\xi_{m,k} = \alpha s$
(1,1)	1.84118
(2,1)	3.05424
(0,1)	3.83171
(3,1)	4.20119
(4,1)	5.31755
(1,2)	5.33144
(5,1)	6.41562
(2,2)	6.70613
(0,2)	7.01559
(6,1)	7.50127
(3,2)	8.01524

3.3.1. Case I: Square cross–section

If we consider the case of a square cross–section, the boundary conditions are

$$z = 0, 1;\ 0 < x < \ell;\ 0 < y < \ell : \quad \tilde{w} = \tilde{T} = 0, \tag{20a}$$

$$x = 0, \ell;\ 0 < y < \ell;\ 0 < z < 1 : \quad \frac{\partial \tilde{w}}{\partial x} = \frac{\partial \tilde{T}}{\partial x} = 0, \tag{20b}$$

$$y = 0, \ell;\ 0 < x < \ell;\ 0 < z < 1 : \quad \frac{\partial \tilde{w}}{\partial y} = \frac{\partial \tilde{T}}{\partial y} = 0. \tag{20c}$$

Thus, the general form of function $f(x, y)$ solving the Helmholtz eigenvalue problem (16) can be expressed as

$$f(x, y) = \cos\left(\frac{m_1\pi}{\ell}x\right)\cos\left(\frac{m_2\pi}{\ell}y\right), \tag{21}$$

where m_1 and m_2 are non–negative integers, while the eigenvalues α are given analytically by

$$\alpha = \frac{\pi}{\ell}\sqrt{m_1^2 + m_2^2}. \tag{22}$$

Therefore, the normal modes are labelled through the pair of integers (m_1, m_2). The symmetry of the square cross–section implies that the modes (m_1, m_2) and (m_2, m_1) are equivalent, as it is mathematically evident from equations (21) and (22). The ordering of such modes according to the increasing eigenvalues is reported in table 1 for the lowest 11 modes.

Table 3
Elliptical cross–section: first 11 eigenvalues αb in increasing order, with the corresponding even (e) or odd (o) normal modes: (e; m, k), (o; m, k).

	$\chi = 9/10$		$\chi = 1/4$
modes	αb	modes	αb
(e; 0, 0)	0	(e; 0, 0)	0
(e; 1, 0)	1.8485646	(e; 1, 0)	1.8832257
(o; 1, 0)	2.0363607	(e; 2, 0)	3.4701287
(e; 2, 0)	3.1870665	(e; 3, 0)	5.0364174
(o; 2, 0)	3.2253344	(e; 4, 0)	6.5946258
(e; 0, 1)	4.0785718	(o; 1, 0)	6.7389286
(e; 3, 0)	4.4108506	(o; 2, 0)	7.8062030
(o; 3, 0)	4.4170182	(e; 5, 0)	8.1482947
(e; 1, 1)	5.4919288	(o; 3, 0)	8.9350656
(e; 4, 0)	5.5884622	(e; 6, 0)	9.6988909
(o; 4, 0)	5.5893372	(o; 4, 0)	10.116229

Table 4
Validation of the numerical values of (Ra_c, α_c) when $Pe \to 0$.

Pe	Ra_c	α_c
10^{-2}	39.4785571021	3.14159634429
10^{-3}	39.4784190030	3.14159269064
10^{-4}	39.4784176220	3.14159265411
10^{-5}	39.4784176082	3.14159265374
0	39.4784176044	3.14159265359

3.3.2. Case II: Circular cross–section

When the lateral confinement is effected with a circular cylinder, the boundary conditions can be written in cylindrical coordinates in the form

$$z = 0, 1; \quad 0 < r < s: \quad \tilde{w} = \tilde{T} = 0, \tag{23a}$$

$$r = s; \quad 0 < z < 1: \quad \frac{\partial \tilde{w}}{\partial r} = \frac{\partial \tilde{T}}{\partial r} = 0. \tag{23b}$$

As a consequence, the general the modes $f(r, \theta)$ obtained by solving the Helmholtz eigenvalue problem (16) are given by

$$f(r, \theta) = J_m(\alpha r) \cos(m\theta), \tag{24}$$

where $J_m(\alpha r)$ is the Bessel function of first kind and order m. In this case, α is determined by solving the equation

$$J'_m(\xi) = 0, \quad \xi = \alpha s. \tag{25}$$

The nonzero values of ξ satisfying equation (25) form a sequence $\{\xi_{m,k} \mid m = 0, 1, 2, 3...; k = 1, 2, 3...\}$ where m is the azimuthal mode number and k the radial mode number. Table 2 shows the first 11 roots of equation (25) in increasing order.

3.3.3. Case III: Elliptical cross–section

Barletta and Storesletten [5] studied, in the case of a Newtonian fluid saturating a porous cylinder, the effect of lateral confinement by a cylindrical wall with elliptical cross-section. In that study, the authors assumed Dirichlet boundary conditions for the Helmholtz problem (16) instead of Neumann boundary conditions. Following the same procedure [5], we use elliptical coordinates, (λ, η), given by

$$x = c \cosh\lambda \cos\eta, \qquad y = c \sinh\lambda \sin\eta, \tag{26}$$

where c is the semi–distance between the foci of the ellipse, $0 \le \lambda < +\infty$ and $0 \le \eta < 2\pi$. The elliptical contour bounding the domain is given by $\lambda = \lambda_0$, the ratio between the semi–axes is given by $d/b = \chi = \tanh\lambda_0$, while $c = b/\cosh\lambda_0$. The limiting case of a circular contour is obtained when $\lambda_0 \to \infty$.

The Helmholtz equation (16) can be solved by separation of variables, with f given by [1, 5]

$$f(\lambda, \eta) = \text{ce}_m(i\lambda; C) \, \text{ce}_m(\eta; C), \tag{27}$$

or

$$f(\lambda, \eta) = i \, \text{se}_m(i\lambda; C) \, \text{se}_m(\eta; C), \tag{28}$$

where $m = 0, 1, 2, \ldots$ and

$$C = \frac{\alpha^2 b^2}{4 \cosh^2 \lambda_0}. \tag{29}$$

Functions ce_m and se_m are the elliptic cosine and elliptic sine, respectively, also called even and odd Mathieu functions of order m.

The boundary condition (16b) can be expressed in elliptical coordinates as

$$\frac{\partial f}{\partial \lambda} = 0, \quad \text{for } \lambda = \lambda_0. \tag{30}$$

Thus, Eqs. (28) and (30) imply that the eigenvalues αs can be computed, for a given aspect ratio χ, as the positive roots of either,

$$\frac{\partial}{\partial \lambda} \text{ce}_m\left(i\lambda; \frac{\alpha^2 b^2}{4 \cosh^2 \lambda_0}\right)\Bigg|_{\lambda=\lambda_0} = 0, \tag{31}$$

$$\frac{\partial}{\partial \lambda} \text{se}_m\left(i\lambda; \frac{\alpha^2 b^2}{4 \cosh^2 \lambda_0}\right)\Bigg|_{\lambda=\lambda_0} = 0, \tag{32}$$

where $\lambda_0 = \text{arctanh}\chi$ and $m = 0, 1, 2, \ldots$.
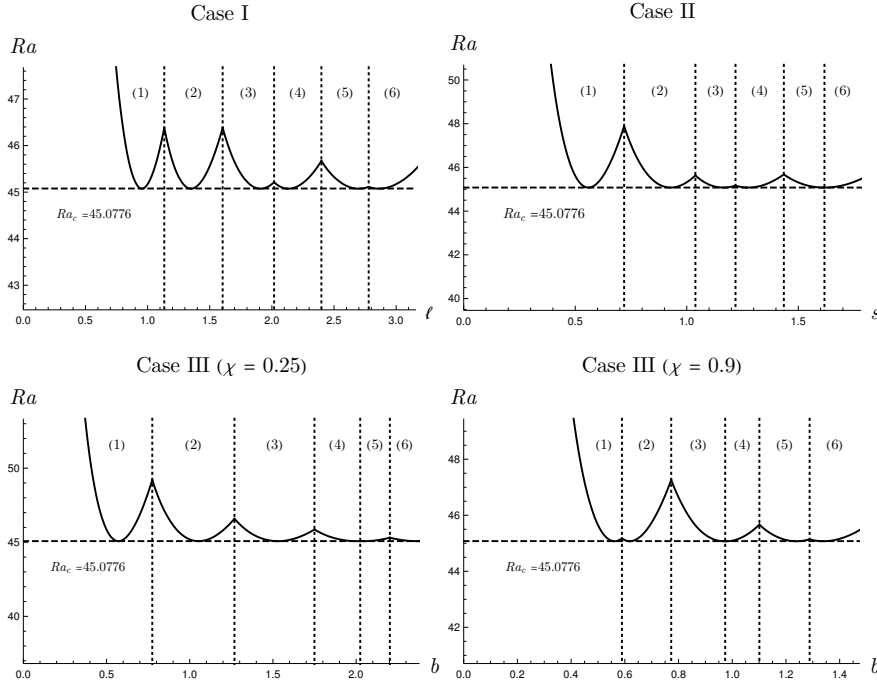Software *Mathematica 12* [17] offers a suitable environment

Figure 2: Marginal stability curves for $n = 1$ and $Pe = 2$; different modes $(1), (2), \ldots$ are labelled according to the ordering defined in tables 1–3
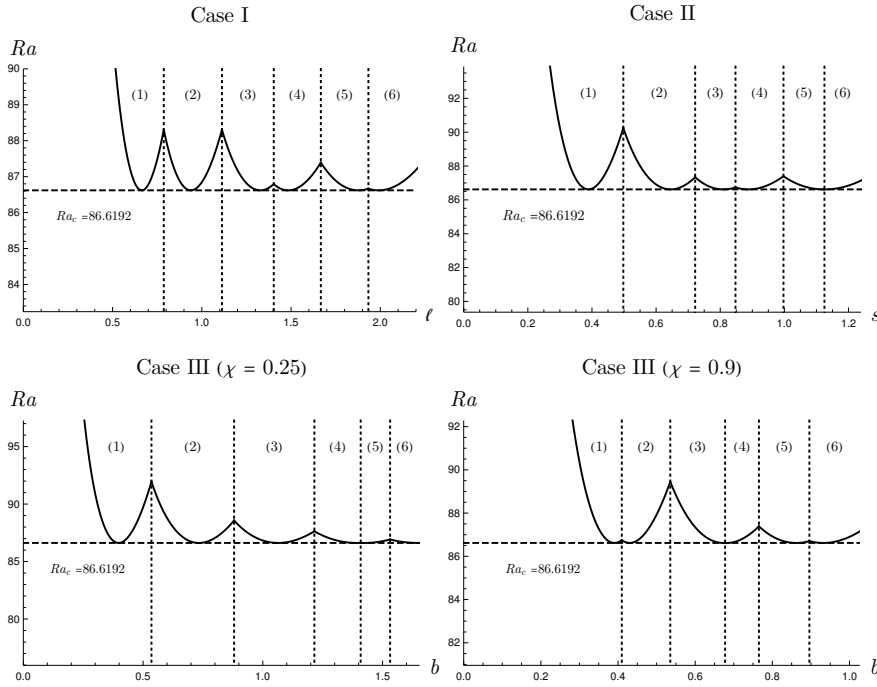

Figure 3: Marginal stability curves for $n = 1$ and $Pe = 6$; different modes $(1), (2), \ldots$ are labelled according to the ordering defined in tables 1–3

for carrying out this computation, by utilising the built–in functions MathieuCPrime, MathieuSPrime, as well as Mathieu CharacteristicA and MathieuCharacteristicB.

The roots of Eqs. (31) and (32) can be ordered so that the eigenvalues α form a monotonic increasing sequence. In analogy with Barletta and Storesletten [5], we employ the

modal notation: $(e; m, k)$ and $(o; m, k)$. Indeed, $(e; m, k)$ denotes the mode associated with the kth root of Eq. (31), for $m, k = 0, 1, 2, \ldots,$. Similarly $(o; m, k)$ is for the kth root of Eq. (32), with $m - 1, k = 0, 1, 2, \ldots$. This ordering of the normal modes, $(e; m, k)$ and $(o; m, k)$, and the associated eigenvalues αb are listed in table 3, for two aspect ratios: $\chi =$
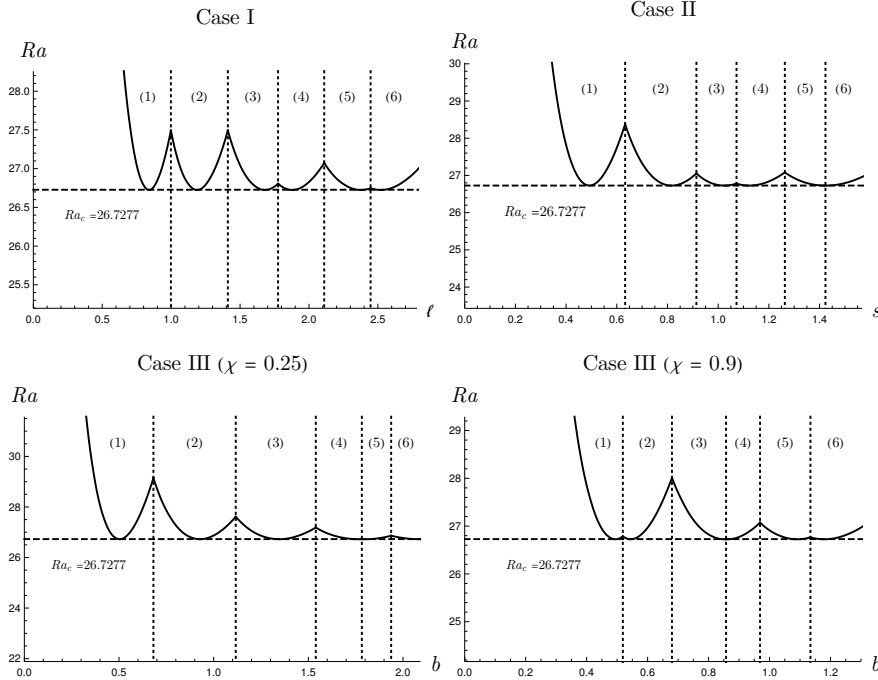
Figure 4: Marginal stability curves for $n = 0.6$ and $Pe = 2$; different modes $(1), (2), \ldots$ are labelled according to the ordering defined in tables 1–3

Figure 5: Marginal stability curves for $n = 0.6$ and $Pe = 6$; different modes $(1), (2), \ldots$ are labelled according to the ordering defined in tables 1–3
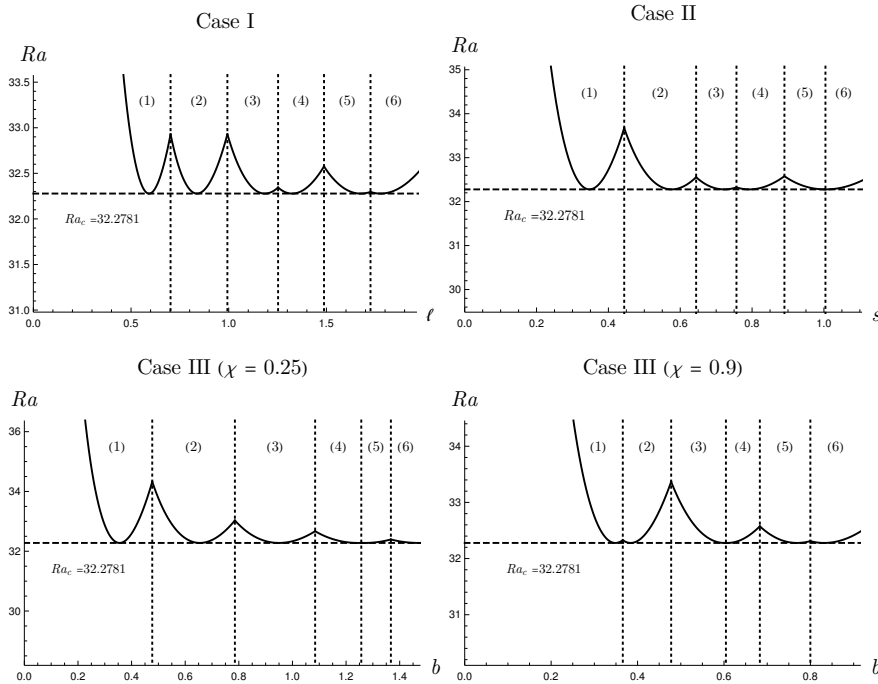
9/10 and $\chi = 1/4$.

4. Critical conditions

By solving equations (17), one may recover the parametric condition which defines the onset of the convective instability, namely the neutral stability condition. That means that, for each pair (n, Pe), one is able to find the neutral stability curve in the plane (α, Ra). The minimum value of Ra along the neutral stability curve yields its critical value, Ra_c. A direct numerical evaluation of Ra_c is possible by deriving equations (17) with respect to α. Thus, one obtains additional equations which lead to an extended eigenvalue prob-

Case I

Case II

Case III ($\chi = 0.25$)

Case III ($\chi = 0.9$)

Figure 6: Marginal stability curves for $n = 2$ and $Pe = 2$; different modes $(1), (2), \ldots$ are labelled according to the ordering defined in tables 1–3

Case I

Case II

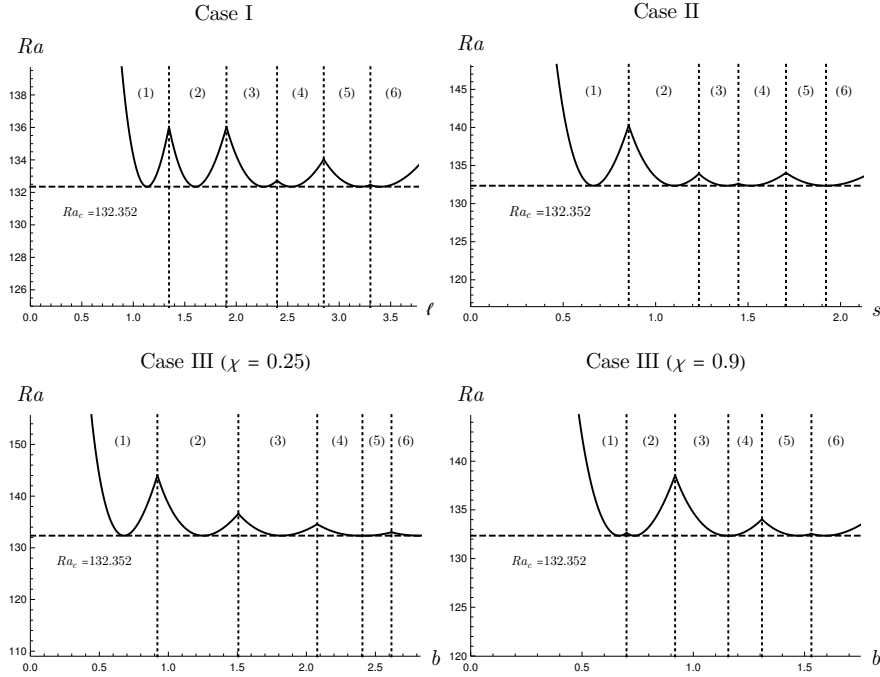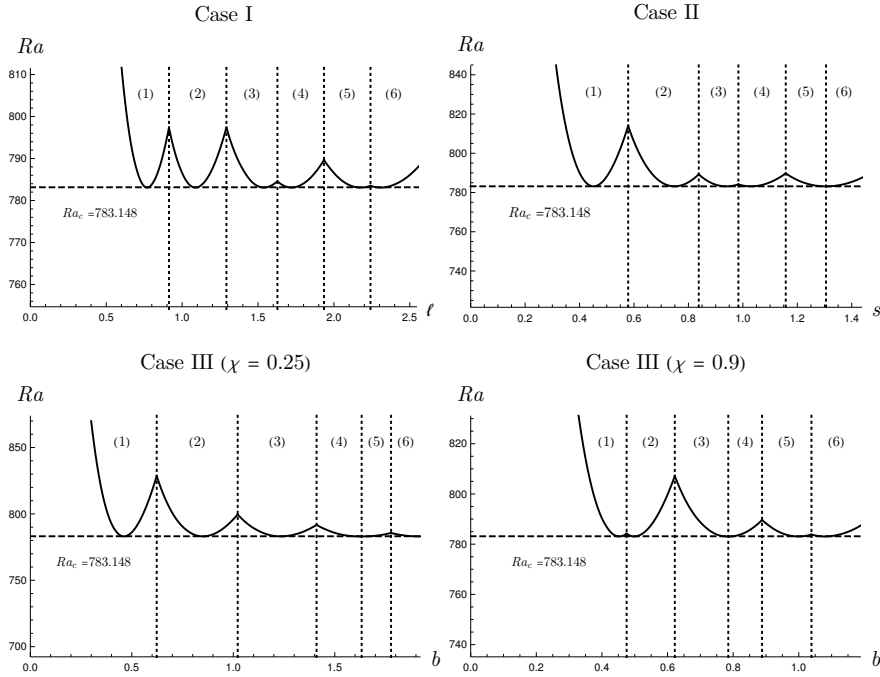Case III ($\chi = 0.25$)

Case III ($\chi = 0.9$)

Figure 7: Marginal stability curves for $n = 2$ and $Pe = 6$; different modes $(1), (2), \ldots$ are labelled according to the ordering defined in tables 1–3

lem, namely

$$W'' - n\alpha^2 W + \frac{Ra}{|Pe|^{n-1}}\,\alpha^2\,\Theta = 0, \qquad (33a)$$

$$\Theta'' - Pe\,\Theta' - \left(\alpha^2 + i\omega\right)\Theta + Pe\,G(z)\,W = 0, \quad (33b)$$

$$\begin{aligned} W_\alpha'' - 2n\,\alpha\,W - n\,\alpha^2\,W_\alpha + \\ 2\frac{Ra}{|Pe|^{n-1}}\,\alpha\,\Theta + \frac{Ra}{|Pe|^{n-1}}\alpha^2\Theta_\alpha = 0, \end{aligned} \quad (33c)$$
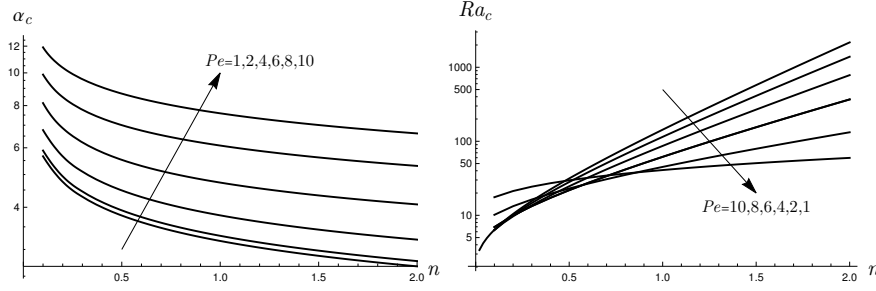
Figure 8: Values of α_c and Ra_c versus n for different Péclet numbers

$$\Theta''_\alpha - Pe\Theta'_\alpha - \left(2\alpha + i\omega_\alpha\right)\Theta - \left(\alpha^2 + i\omega\right)\Theta_\alpha + Pe\,G(z)\,W_\alpha = 0, \quad \text{(33d)}$$

$$z = 0, 1: \quad W = W_\alpha = 0, \quad \Theta = \Theta_\alpha = 0, \quad \text{(33e)}$$

where $W_\alpha = \partial W/\partial\alpha$, $\Theta_\alpha = \partial\Theta/\partial\alpha$ and $\omega_\alpha = \partial\omega/\partial\alpha$. Equations (33c) and (33c) have been obtained with the understanding that (n, Pe) are fixed and that $\partial Ra/\partial\alpha$ is zero as we are seeking the minimum of Ra along the neutral stability curve in the (α, Ra) plane. Hence, the solution of the extended eigenvalue problem (33) yields the eigenvalues α, Ra, ω and ω_α corresponding to a prescribed pair (n, Pe). In particular, the eigenvalue Ra is to be intended as the critical value Ra_c for the onset of instability, and α is the critical wavenumber α_c.

The method adopted to solve the eigenvalue problem (33) is the shooting method [15, 3]. Such a method consists in transforming the boundary value problem into an initial value problem by the introduction of additional initial conditions at $z = 0$ and then marching the solution to $z = 1$ in such a way as to satisfy the end conditions (33e) at $z = 1$. When one takes the limit $Pe \to 0$ in the Newtonian case ($n = 1$), the classical Horton–Rogers–Lapwood (HRL) problem is retrieved [11]. Then, this case can be employed as a benchmark to test the accuracy of the numerical method. The analytical solution of the HRL problem yields $Ra_c = 4\pi^2$ and $\alpha_c = \pi$ [11]. A comparison between the numerical data obtained for extremely small Péclet numbers and $n = 1$ and the analytical solution of the HRL problem is reported in table 4. The numerical data are displayed with 12 significant figures and an extremely good agreement, with 9 coincident figures, can be observed already for $Pe = 10^{-4}$. Figure 8 shows the influence of the power–law index n on the critical values of α and Ra for fixed values of Pe.

All the numerical calculations are carried out by using the Software *Mathematica 12* [17]. By using the built-in function called *NDSolve* one can solve a wide class of differential equations systems. In order to assess the accuracy of the computations, we perform a convergence analysis by choosing decreasing step sizes inside *NDSolve*, as well as the adaptive step size method used as a default in *NDSolve*. Such an analysis of convergence is reported in Table 5 through the

values of the critical wavenumber and of the critical Rayleigh number.

Table 5
Values of Ra_c and α_c obtained numerically by considering different step sizes for $Pe = 4$ and $n = 0.6$

Step size	$\hat{\alpha}_c$	$\hat{Ra}_c$
0.5	4.28892481141	27.3269196664
0.1	4.28892481141	27.3269196664
0.05	4.28892481184	27.3269196612
0.01	4.28892481184	27.3269196612
0.005	4.28892481184	27.3269196612
Adaptive	4.28892481184	27.3269196612

In order to illustrate the critical temperature difference leading to the instability for a specific fluid, we employed the properties of the fluid and of the porous medium employed in Experiment 5 described in Petrolo et al. [12]. In particular, we consider a porous medium with porosity 0.5 and $H = 0.5$ m. In this case, we have a temperature difference of 5.60 K at the onset of the instability.

Moreover, in Fig. 9, we plot the the most unstable modes for the elliptic case with $\xi = 9/10$. This case is endowed with a lower geometrical symmetry with respect to the circular case, while it allows an analytical expression of the eigenmodes in terms of nontrivial special functions.

5. Neutral stability condition

Figures 2 and 3 show the neutral stability curves for the Newtonian case ($n = 1$), with $Pe = 2$ and $Pe = 6$ respectively. The curves are presented for each of the three cases defined in Section 3.3. For the elliptical cross–section case, two different aspect ratios between the two semi–axis are considered. The numbers above the curves denote the modes corresponding to each branch. All these curves are generated for the lower six modes of perturbation. The critical values of Ra shown in these plots coincide with those reported by [8] as well as by Barletta et al. [4].

Figures 4–7 show the neutral stability curves for non–Newtonian flows ($n \neq 1$). In particular, figures 4 and 5 are relative to a pseudoplastic fluid, while figures 6 and 7 are drawn for a dilatant fluid. Again the results are present for
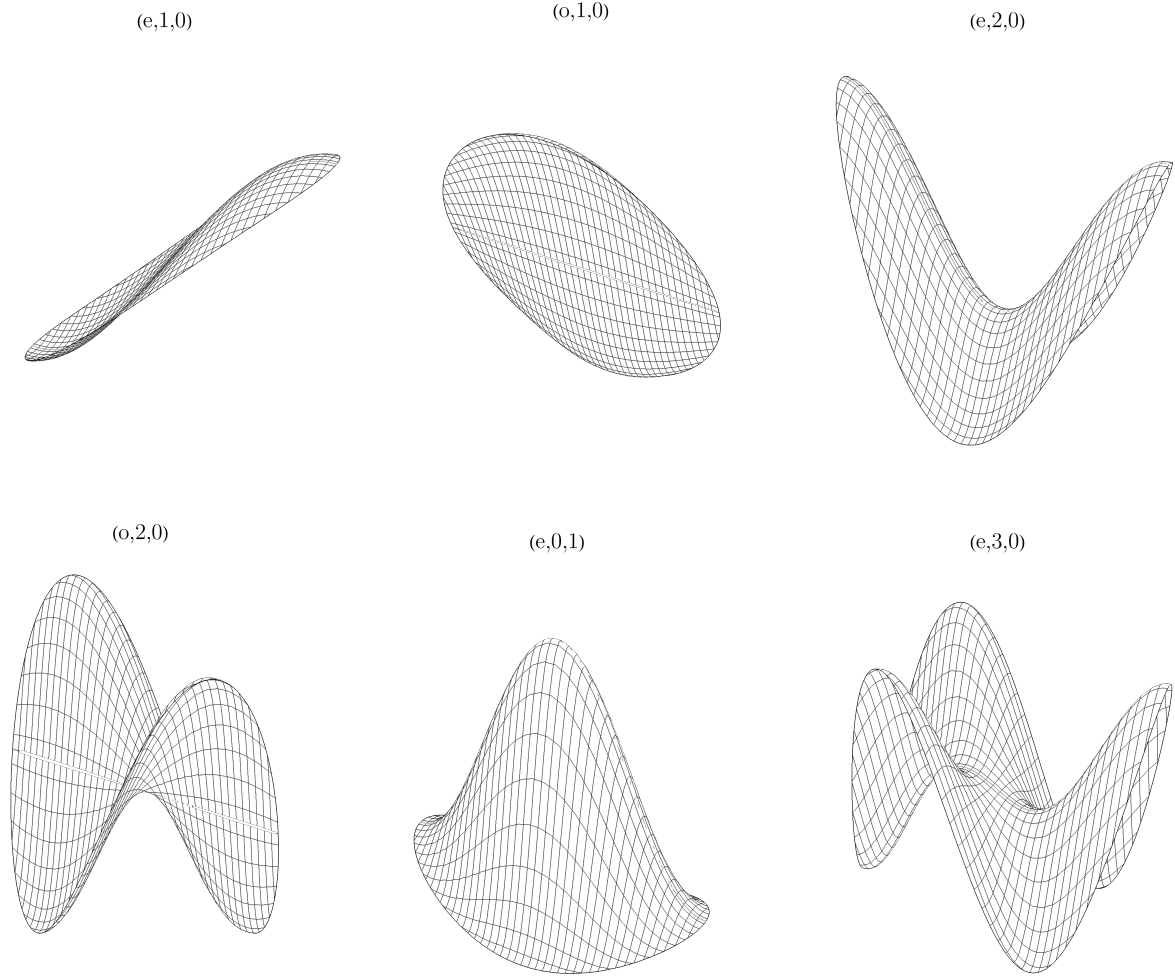
(e,1,0) (o,1,0) (e,2,0)

(o,2,0) (e,0,1) (e,3,0)

Figure 9: Plots of the eigenfunctions for an elliptic cylinder with $\xi = 9/10$ relative to the first 6 normal modes

fixed Pe and n and for three different geometries of the cylinder cross–section. The critical values of Ra displayed in these figures are in perfect agreement with those reported in Barletta and Storesletten [6]. The lateral confinement changes significantly the selection of the modes and consequently the pattern selection on the onset of instability. However, the critical values of Ra and α just depend on n and Pe, as they are determined by the solution of equations (33), while they are not influenced by the geometry of the sidewall. Therefore, for the sake of conciseness, we refer the reader to Barletta and Storesletten [6] for a thorough discussion of the critical values of Ra and α and of their dependence on n and Pe. An interesting asymptotic solution can be found for $|Pe| \gg 1$, albeit this solution was not reported in the paper by Barletta and Storesletten [6].

6. The asymptotic solution for large Péclet numbers

When $|Pe|$ becomes very large, the convection cells at the onset of instability gradually display a boundary layer structure, as they tend to be confined to a small region close to either the lower boundary, $z = 0$, or the upper boundary, $z = 1$, depending on the sign of Pe.

We have already noted in Section 3.2 that the eigenvalue problem (17) is symmetric under flow reversal, $Pe \to -Pe$. In the forthcoming analysis, the Péclet number Pe is assumed as negative, thus relying on the above mentioned symmetry to infer the behaviour when Pe is positive. For $Pe < 0$ and $|Pe| \gg 1$, the convective cells concentrate close to the lower boundary, $z = 0$. First of all, we rescale the quantities z, W, Ra and α by defining

$$\hat{z} = z\,|Pe|, \quad \hat{W} = \frac{W}{|Pe|}, \quad \hat{Ra} = \frac{Ra}{|Pe|^n}, \quad \hat{\alpha} = \frac{\alpha}{|Pe|}. \quad (34)$$

Then, by considering $Pe < 0$ and $\omega = 0$, equations (17) can be rewritten as

$$\frac{\mathrm{d}^2 \hat{W}}{\mathrm{d}\hat{z}^2} - n\,\hat{\alpha}^2\,\hat{W} + \hat{Ra}\,\hat{\alpha}^2\,\Theta = 0, \quad (35\mathrm{a})$$

$$\frac{\mathrm{d}^2 \Theta}{\mathrm{d}\hat{z}^2} + \frac{\mathrm{d}\Theta}{\mathrm{d}\hat{z}} - \hat{\alpha}^2\,\Theta - \frac{e^{-\hat{z}}}{e^{-|Pe|} - 1}\,\hat{W} = 0, \quad (35\mathrm{b})$$
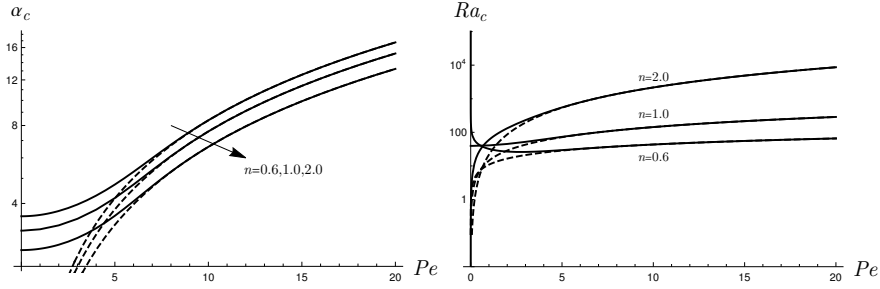
Figure 10: Critical values of α_c and Ra_c versus Pe for different values of n. The solid lines are obtained by solving equations (33), while the dashed lines are relative to the asymptotic solution valid for $|Pe| \gg 1$

Table 6
Sensitivity of $\hat{\alpha}_c$ and $\hat{Ra}_c$ to the choice of $\hat{z}_{\max}$ for $n = 0.1$.

$\hat{z}_{\max}$	$\hat{\alpha}_c$	$\hat{Ra}_c$
10	1.19032239700	5.06444512579
11	1.18047438202	5.05575866872
12	1.17489331882	5.05149305271
13	1.17181039419	5.04941766775
14	1.17014306733	5.04841472535
15	1.16925621114	5.04793225624
16	1.16879049859	5.04770083714
17	1.16854834716	5.04759003274
18	1.16842341049	5.04753703493
19	1.16835934958	5.04751170145
20	1.16832667007	5.04749959597
21	1.16831007088	5.04749381254
22	1.16830167066	5.04749104979
23	1.16829743338	5.04748973009
24	1.16829530211	5.04748909972
25	1.16829423286	5.04748879863
26	1.16829369767	5.04748865481
27	1.16829343035	5.04748858611
28	1.16829329708	5.04748855330
29	1.16829323076	5.04748853763
30	1.16829319781	5.04748853015

Table 7
Comparison between the asymptotic analysis ($|Pe| \gg 1$) and the solution of equations (33) with $Pe = 20$: critical values of $\hat{\alpha}$ and $\hat{Ra}$

n	$\hat{\alpha}_c$	$\hat{\alpha}_c$ ($|Pe| \gg 1$)	$\hat{Ra}_c$	$\hat{Ra}_c$ ($|Pe| \gg 1$)
0.1	1.16833	1.16829	5.04750	5.04749
0.2	1.02929	1.02929	6.56943	6.56942
0.4	0.904532	0.904532	8.92619	8.92619
0.6	0.837517	0.837517	10.9049	10.9049
0.8	0.792457	0.792457	12.6901	12.6901
1.0	0.758867	0.758867	14.3522	14.3522
1.2	0.732280	0.732280	15.9270	15.9270
1.4	0.710389	0.710389	17.4357	17.4357
1.6	0.691853	0.691853	18.8921	18.8921
1.8	0.675827	0.675827	20.3058	20.3058
2.0	0.661746	0.661746	21.6837	21.6837

Now one may solve equations (36) by adapting the shooting method mentioned in Section 4 to a situation where the eigenvalue problem is defined over a semi–infinite range, $\hat{z} \geqslant 0$. To this aim, we first develop the numerical solution of the system (36) by assuming that the conditions for $\hat{z} \to +\infty$ hold, in fact, for a sufficiently large $\hat{z} = \hat{z}_{\max}$. Then, the sensitivity to the choice of $\hat{z}_{\max}$ is tested by gradually increasing its value. Table 6 illustrates the test for a strongly pseudo–plastic fluid ($n = 0.1$), as this condition turned to display a very large sensitivity to the choice of $\hat{z}_{\max}$. This table shows that with $\hat{z}_{\max} = 25$ one achieves a 6 figures accuracy in the evaluation of both $\hat{\alpha}_c$ and $\hat{Ra}_c$.

On account of equations (34) and (36), we can conclude that, when $|Pe| \gg 1$, the neutral stability value of Ra is proportional to $|Pe|^n$, that is

$$Ra = \hat{Ra}\,|Pe|^n. \tag{37}$$

Table 7 reports the critical values of $\alpha/|Pe|$ and $Ra/|Pe|^n$ evaluated by solving equations (33) with $Pe = 20$. In the same table, these data are compared with the critical values of $\hat{\alpha}$ and $\hat{Ra}$ obtained by the numerical solution of equations (36) for the asymptotic case $|Pe| \gg 1$. The agreement is extremely good especially for $n \geqslant 0.4$. In every case, the data with $Pe = 20$ and $|Pe| \gg 1$ coincide within at least 5 significant figures. A useful comparison is one between the trends of α_c and Ra_c obtained by solving equations (33) with those

$$\hat{z} = 0, |Pe| : \quad \Theta = \hat{W} = 0. \tag{35c}$$

By taking the limit $|Pe| \to \infty$, equations (35) yield

$$\frac{\mathrm{d}^2\hat{W}}{\mathrm{d}\hat{z}^2} - n\,\hat{\alpha}^2\,\hat{W} + \hat{Ra}\,\hat{\alpha}^2\,\Theta = 0, \tag{36a}$$

$$\frac{\mathrm{d}^2\Theta}{\mathrm{d}\hat{z}^2} + \frac{\mathrm{d}\Theta}{\mathrm{d}\hat{z}} - \hat{\alpha}^2\,\Theta + e^{-\hat{z}}\,\hat{W} = 0, \tag{36b}$$

$$\Theta(0) = \hat{W}(0) = 0. \tag{36c}$$

$$\lim_{\hat{z}\to+\infty}\Theta = \lim_{\hat{z}\to+\infty}\hat{W} = 0. \tag{36d}$$

obtained by employing the asymptotic solution data given by table 7. Figure 10 illustrates such trends, where the solid lines are relative to the solution of equations (33), while the dashed lines denote the asymptotic solution for $|Pe| \gg 1$. An evident overlapping between the solid and the dashed lines is shown for $|Pe| > 10$ meaning that, in this range, the asymptotic solution can be considered as a reliable approximation. We also note that, for a Newtonian fluid ($n = 1$), Homsy and Sherwood [8] reported the values $\hat{\alpha}_c = 0.759$ and $\hat{Ra}_c = 14.3$, respectively. In fact, the agreement with the data displayed in table 7 is fair, but we note that Homsy and Sherwood [8] did not describe explicitly the procedure followed to obtain their results.

7. Conclusions

The effects of the lateral confinement with impermeable adiabatic sidewalls on the onset of thermoconvective instability in a porous medium have been studied. A porous layer saturated by a power–law fluid has been considered. The layer is laterally bounded by a vertical cylindrical wall with arbitrary cross-section and it is subject to a vertical base throughflow. The permeable horizontal boundaries of the porous cylinder are kept at different uniform temperatures, with heating from below, so that the vertical base through-flow may display an instability of the Rayleigh–Bénard type. The power–law Darcy's model of momentum transfer has been employed to study the onset of the instability to small–amplitude perturbations. The dimensionless parameters driving the instability are the power–law index, n, the Péclet number of the base throughflow, Pe, and the Darcy–Rayleigh number, Ra. Normal mode perturbations are identified by the wavenumber, α, whose values are constrained by the geometry of the sidewall boundary. Thus, for a given geometry, only a discrete sequence of wavenumbers is allowed, which depends on the geometry of the sidewall. The main features of the instability reported in our study are the following:

- The rheology of the saturating fluid, *i.e.*, its power–law index n does not influence the sequence of the allowed wavenumbers, α. This sequence is uniquely determined by solving the two–dimensional Helmholtz eigenvalue problem with Dirichlet boundary conditions defined in the cylinder horizontal cross–section. With this aim in mind, we have considered three sample geometries of the cylinder cross–section: square, circle and ellipse.

- The neutral stability curve in the (α, Ra) parametric plane depends only on n and Pe, while the geometry of the sidewall just contribute the selection of the allowed wavenumbers.

- There exists an asymptotic solution of the neutral stability problem which holds for $|Pe| \gg 1$. In this regime, the convection cells arising at the onset of the instability form a boundary layer structure. Roughly

speaking, numerical data show that such a solution is reliable when Pe is approximately larger than 10.

CRediT authorship contribution statement

P.V. Brandão: Methodology, Conceptualisation, Writing - original draft, Validation. **M. Celli:** Methodology, Conceptualisation, Writing - original draft, Validation. **A. Barletta:** Methodology, Conceptualisation, Writing - original draft, Validation. **L. Storesletten:** Methodology, Conceptualisation, Writing - original draft, Validation.

References

[1] Abramowitz, M., Stegun, I.A., 1948. Handbook of Mathematical Functions with Formulas, Graphs, and Mathematical Tables. volume 55. US Government Printing Office.

[2] Alves, L.S.d.B., Barletta, A., 2013. Convective instability of the Darcy–Bénard problem with through flow in a porous layer saturated by a power–law fluid. International Journal of Heat and Mass Transfer 62, 495–506.

[3] Barletta, A., 2019. Routes to Absolute Instability in Porous Media. Springer, New York.

[4] Barletta, A., di Schio, E.R., Storesletten, L., 2010. Convective roll instabilities of vertical throughflow with viscous dissipation in a horizontal porous layer. Transport in Porous Media 81, 461–477.

[5] Barletta, A., Storesletten, L., 2015. Onset of convection in a vertical porous cylinder with a permeable and conducting side boundary. International Journal of Thermal Sciences 97, 9–16.

[6] Barletta, A., Storesletten, L., 2016. Linear instability of the vertical throughflow in a horizontal porous layer saturated by a power-law fluid. International Journal of Heat and Mass Transfer 99, 293–302.

[7] Di Federico, V., Pinelli, M., Ugarelli, R., 2010. Estimates of effective permeability for non-newtonian fluid flow in randomly heterogeneous porous media. Stochastic Environmental Research and Risk Assessment 24, 1067–1076.

[8] Homsy, G.M., Sherwood, A.E., 1976. Convective instabilities in porous media with through flow. AIChE Journal 22, 168–174.

[9] Horton, C.W., Rogers Jr, F.T., 1945. Convection currents in a porous medium. Journal of Applied Physics 16, 367–370.

[10] Lapwood, E.R., 1948. Convection of a fluid in a porous medium, in: Mathematical Proceedings of the Cambridge Philosophical Society, Cambridge University Press. pp. 508–521.

[11] Nield, D.A., Bejan, A., 2017. Convection in Porous Media. 5th ed., Springer, New York.

[12] Petrolo, D., Chiapponi, L., Longo, S., Celli, M., Barletta, A., Di Federico, V., 2020. Onset of darcy–bénard convection under throughflow of a shear–thinning fluid. J. Fluid Mech 889, R2.

[13] Prats, M., 1966. The effect of horizontal fluid flow on thermally induced convection currents in porous mediums. Journal of Geophysical Research 71, 4835–4838.

[14] Shenoy, A.V., 1994. Non–Newtonian fluid heat transfer in porous media. Advances in Heat transfer 24, 102–191.

[15] Straughan, B., 2008. Stability and Wave Motion in Porous Media. Springer, New York.

[16] Sutton, F.M., 1970. Onset of convection in a porous channel with net through flow. The Physics of Fluids 13, 1931–1934.

[17] Wolfram Research, Inc., . Mathematica 12.0 Champaign, IL, 2019, www.wolfram.com/mathematica.